J. Fluid Mech. (2012), *vol.* 693, *pp.* 473–499. © Cambridge University Press 2012
doi:10.1017/jfm.2011.543

Dynamic pitching of an elastic rectangular wing in hovering motion

Hu Dai[1], **Haoxiang Luo**[1]† **and James F. Doyle**[2]

[1] Department of Mechanical Engineering, Vanderbilt University, 2301 Vanderbilt Place, Nashville, TN 37235-1592, USA

[2] School of Aeronautics and Astronautics, Purdue University, West Lafayette, IN 47907-2045, USA

(Received 16 August 2011; revised 19 October 2011; accepted 9 December 2011; first published online 17 January 2012)

In order to study the role of the passive deformation in the aerodynamics of insect wings, we computationally model the three-dimensional fluid–structure interaction of an elastic rectangular wing at a low aspect ratio during hovering flight. The code couples a viscous incompressible flow solver based on the immersed-boundary method and a nonlinear finite-element solver for thin-walled structures. During a flapping stroke, the wing surface is dominated by non-uniform chordwise deformations. The effects of the wing stiffness, mass ratio, phase angle of active pitching, and Reynolds number are investigated. The results show that both the phase and the rate of passive pitching due to the wing flexibility can significantly modify the aerodynamics of the wing. The dynamic pitching depends not only on the specified kinematics at the wing root and the stiffness of the wing, but also greatly on the mass ratio, which represents the relative importance of the wing inertia and aerodynamic forces in the wing deformation. We use the ratio between the flapping frequency, ω, and natural frequency of the wing, ω_n, as the non-dimensional stiffness. In general, when $\omega/\omega_n \leqslant 0.3$, the deformation significantly enhances the lift and also improves the lift efficiency despite a disadvantageous camber. In particular, when the inertial pitching torque is assisted by an aerodynamic torque of comparable magnitude, the lift efficiency can be markedly improved.

Key words: flow–structure interactions, swimming/flying, vortex shedding

1. Introduction

The membranous wings of flying insects are usually highly flexible and thus display considerable passive deformations during flight (Wootton 1981, 1992). In general, the deformation pattern of an insect wing can be described by bending and spanwise twist around the wing axis. These deformation features alter the instantaneous angle of attack, speed of stroke, and pitching velocity (angular velocity around the spanwise axis). Additionally, chordwise bending may create a dynamic camber for the wing. Thus, the wing deformation has significant aerodynamic consequences. Early observations of the insect wing movement have led to conjecture that the deformation may improve the aerodynamic performance of insect wings (e.g. Ennos

† Email address for correspondence: haoxiang.luo@vanderbilt.edu

https://doi.org/10.1017/jfm.2011.543 Published online by Cambridge University Press

1988*a*). However, previous studies on the low-Reynolds-number aerodynamics of insect flight have mainly focused on rigid wings (e.g. Dickinson, Lehmann & Sane 1999; Sun & Tang 2002; Wang 2005). It was only recently that the effect of structural flexibility became an important topic, which is partly due to the renewed interest in biomimetic air vehicles and partly due to modern advances in numerical simulations and experimental techniques. Among the existing studies on the aerodynamics of flexible wings, several have shown that by adding some level of flexibility to a rigid flapping wing, the performance of the wing can be significantly improved. For example, Vanella *et al.* (2009) used a two-link model to represent the chordwise flexibility. Their two-dimensional (2D) simulation shows that the wing deformation can increase the lift-to-drag ratio by 28 % and the lift-to-power ratio by 39 % and that the best performance is obtained when the flapping frequency is a fraction of the natural frequency of the wing structure. Using a similarly simplified model, Eldredge, Toomey & Medina (2010) investigated the effect of chordwise deformation over a range of hovering kinematic parameters. They found that a mildly flexible wing consistently has better power efficiency compared to the rigid wing for a wide range of phase differences between pitching and wing translation. In addition to these computational studies, experiments performed in liquid (e.g. Prempraneerach, Hover & Triantafyllou 2003; Heathcote & Gursul 2007) and in air (Ramananarivo, Godoy-Diana & Thiria 2011) showed that the chordwise deformation can significantly enhance the propulsive force and efficiency of the wing. For a more extensive review of the recent experimental and computational studies on flexible wings, readers are referred to Kang *et al.* (2011).

A flapping wing is subject to an inertial force due to its own mass and also to the aerodynamic forces from the surrounding air. Previous studies suggest that both forces may be able to cause an insect wing to deform. For example, Ennos (1988*a*) measured the force manually applied on the wings of two species of flies, and he concluded that the aerodynamic forces experienced by the insect wings during flight would be sufficient to produced the observed values of wing twist and camber. In another study, Ennos (1988*b*) measured the mass distribution and determined the torsional axis of three species of flies, and the result shows that the inertial effect alone could develop the pitching velocity observed at stroke reversal. Combes & Daniel (2003) compared vibrations of the excised hawkmoth wing in air and in helium (15 % of the air density) and noticed that the deformation patterns in the two cases are close to each other. Their result suggests that the hawkmoth wing is mainly deformed by the wing inertia during stroke. Whether it is the wing inertia or the aerodynamic forces that cause the wing deformation may determine the timing of the deformation. The reason is that there is a phase difference between the inertial force and the aerodynamic forces in a flapping cycle. Roughly speaking, the inertial force reaches its maximum around stroke reversal when the wing has the highest acceleration, while the aerodynamic forces peak around mid-stroke when the wing has the fastest translation. If the aerodynamic forces are strong enough, they may maintain the passive pitching caused by the inertial effects at stroke reversal (Ennos 1988*a*). Though these qualitative considerations make sense, a detailed study is needed to find out the exact timing and contribution of all the forces involved. Furthermore, it is necessary to include fluid–structure interaction in such a study and to simultaneously investigate the aerodynamic consequences of the wing deformation. Currently, the relative roles of the inertial and aerodynamic torques in the deformation and performance of flapping wings are still elusive.

Since the aerodynamic pressure scales with ρU^2, where ρ is the fluid density and U is the characteristic velocity of the wing, and the inertial force per unit

https://doi.org/10.1017/jfm.2011.543 Published online by Cambridge University Press

area scales with $\rho_s hU^2/\mathscr{L}$, where ρ_s is the density of the wing material, h is the membrane thickness (collectively, $\rho_s h$ is the surface density), and $\mathscr{L}$ is the characteristic length scale, the ratio between the inertial effect and the aerodynamic effect is thus represented by the mass ratio $\rho_s h/(\rho\mathscr{L})$, denoted by m^* here. In the current study, we choose the chord length c for the length scale. From the previously available insect data, Yin & Luo (2010) estimated that the mass ratio is around $m^* = 1$ for the dragonfly used in Chen, Chen & Chou (2008) and around $m^* = 5$ for the hawkmoth used in Combes & Daniel (2003). Using the mass distribution measured by Ennos (1988*b*), we estimate that the mass ratio of the hoverfly in his experiment is around $m^* = 0.5$ near the wing tip. These estimates give us a sense of the relative importance of the inertial force in the wing deformation of these insects and will form the basis for the choice of the mass ratio in the current study.

In an earlier study, Yin & Luo (2010) performed a numerical simulation of the fluid–structure interaction for a wing section and studied the effect of the wing inertia in hovering flight. By comparing $m^* = 1$, 5, and 25, they found that the wing at low mass ratios can achieve much higher lift per unit power and it does so by yielding itself to the aerodynamic forces and reducing the drag force. In addition, significant phase difference in the deformation of the wing was found between the high-mass-ratio and low-mass-ratio cases. However, their analyses of the inertial/aerodynamic torques and passive wing rotation are rather qualitative. In addition, the wing-root kinematics in their study is limited to symmetric pitching, while adding a prescribed phase angle would allow one to compensate the passive pitching due to deformation and thus to compare the wing performance at constant phase angle. Moreover, their study is limited to two dimensions. In the present study, we consider a much more computationally intensive three-dimensional (3D) model, which is motivated by the fact that many of the insect wings have a low aspect ratio and the tip vortex and spanwise flow play important roles in the aerodynamics of the wings (Ellington *et al.* 1996; Birch & Dickinson 2001).

In the present work, we use a flexible rectangular plate at a low aspect ratio to model the effect of chordwise deformation in hovering flight. The plate revolves around a pivot point and at the same time rotates around its rigid leading edge to mimic stroke and global pitching (active pitching at the wing root) of a real insect wing. The 3D fluid–structure interaction is solved by coupling an immersed-boundary flow solver and a nonlinear finite-element method for the structural dynamics. By systematically varying the wing stiffness, mass ratio, and phase of the global pitching, we hope to gain insight into the interplay among the inertial, aerodynamic, and elastic forces in the flapping flight. The paper is organized as follows. The problem is described in § 2; the numerical method, validation, and study of grid convergence are described in § 3; the simulation and result analysis are presented in § 4; and finally conclusions are given in § 5.

2. Problem formulation

We consider a thin rectangular plate of aspect ratio 2 which rotates around the z-axis while pitching around its leading edge as shown in figure 1(*a,b*). The plate has a chord length c and a spanwise width of $L = 2c$. The leading edge is rigid, but the bulk surface of the plate is flexible and is both homogeneous and isotropic (figure 1*c*). The wing is activated by the torques at the pivot point so that the leading edge undergoes

https://doi.org/10.1017/jfm.2011.543 Published online by Cambridge University Press

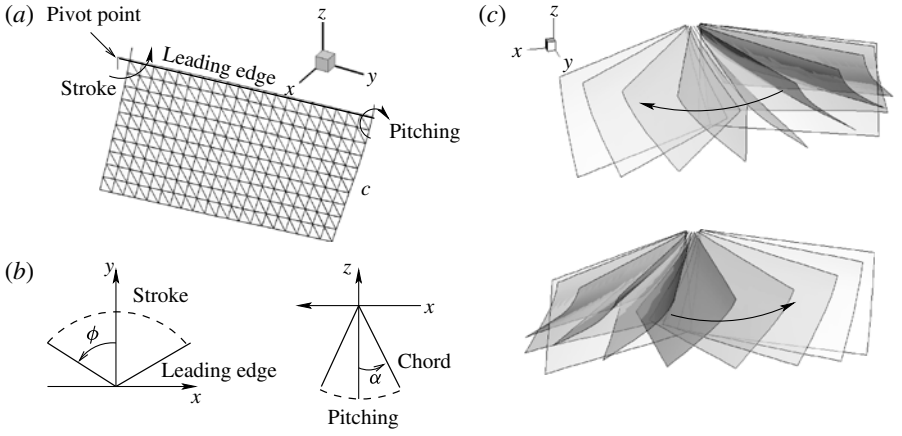


FIGURE 1. The wing model used in the current study. (*a*) Configuration and mesh of a rectangular wing. (*b*) Sketch of the specified kinematics. (*c*) Instantaneous wing deformation during a stroke.

two degrees-of-freedom rotations described by

$$\phi = \frac{A_\phi}{2} \sin\left(2\pi f t + \frac{\pi}{2}\right) \tag{2.1}$$

$$\alpha = \frac{A_\alpha}{2} \sin\left(2\pi f t + \varphi\right), \tag{2.2}$$

where f is the frequency, ϕ is the stroke angle defined as the angle between the leading edge and the y-axis, α is the active pitching angle specified at the wing root, φ is the phase angle between wing stroke and the pitching motion with $\varphi = 0$ corresponding to symmetric pitching. A_ϕ and A_α are the amplitudes of stroke and pitching, respectively. The kinematics of the leading edge is shown in figure 1(*a,b*). The origin of the coordinate system is located at the pivot point, and the length of the wing arm (from the pivot point to the inner edge of the plate) is equal to $0.1c$. In the current study, we choose $A_\phi = 2\pi/3$ and $A_\alpha = \pi/3$, which are in the range of real insect data (e.g. Wang *et al.* 2003; Hedrick, Cheng & Deng 2009).

The fluid is Newtonian and is governed by the viscous incompressible Navier–Stokes equations. No-slip and no-penetration conditions for the fluid are imposed on the plate surface, and the plate is subject to the hydrodynamic traction differential $\boldsymbol{f} = \left[\boldsymbol{\sigma}^{(+)} - \boldsymbol{\sigma}^{(-)}\right] \cdot \boldsymbol{n}$, where $\boldsymbol{\sigma}$ is the hydrodynamic stress tensor, $\boldsymbol{n}$ is the surface normal, and plus/minus denote the two sides of the plate. The plate is characterized by its surface density $\rho_s h$, where ρ_s is the density of the solid and h is the thickness of the plate, Poisson's ratio ν_p, and the flexural stiffness EI, where E is Young's modulus and $I = h^3/12$ is the second moment of area of the cross-section. Poisson's ratio is assumed to be $\nu_p = 0.25$. In addition to the phase angle φ, the other non-dimensional groups of the problem include the Reynolds number, mass ratio, and frequency ratio of the plate, which are given by

$$Re = \frac{Uc}{\nu}, \quad m^* = \frac{\rho_s h}{\rho c}, \quad \omega^* = \frac{2\pi f}{\omega_n}, \tag{2.3}$$

where U is the characteristic velocity, chosen to be the mean tip velocity of the leading edge, $U = 2A_\phi f(L + 0.1c) = 8.797cf$, ρ and ν are the fluid density and

https://doi.org/10.1017/jfm.2011.543 Published online by Cambridge University Press

viscosity, respectively, and $\omega_n = (1.8751^2/c^2)\sqrt{EI/\rho_s h}$ is the first natural frequency of the plate using the classical Euler–Bernoulli beam theory. Note that when the other parameters are fixed, $\omega^* = 0$ corresponds to a rigid plate, and as ω^* is increased, the plate becomes more flexible. An alternative way of normalizing the bending rigidity is to use the dynamic pressure, ρU^2 (e.g. Prempraneerach *et al.* 2003). The approach in (2.3) is chosen here since it gives a direct measure of how close the flapping frequency is to the resonant frequency of the wing structure.

To evaluate the wing performance, we define the lift F_L as the z-component of the resultant fluid force, and the drag F_D as the force component in the xy-plane and perpendicular to the leading edge. In each half-stroke, the drag is positive when it is against the translation of the leading edge. The aerodynamic power P is computed by integrating the dot product of the fluid force and local velocity of the wing over the entire wing surface. The lift and drag coefficients, C_L and C_D, are defined by normalizing the corresponding force with $(1/2)\rho U^2 cL$, and the power coefficient, C_P, is defined by normalizing P with $(1/2)\rho U^3 cL$.

3. Numerical method for the fluid–structure interaction

3.1. *Numerical method*

The computational fluid–structure interaction is achieved by coupling a second-order, Cartesian-grid-based immersed-boundary flow solver and a nonlinear finite-element structural solver. Both solvers and their coupling are described in detail in Luo *et al.* (2010, 2011). Only brief descriptions are provided here.

The governing equations for the flow are discretized on a non-uniform Cartesian grid that covers the entire computational domain, including both the fluid region and the plate. The primary variables, the fluid velocity and pressure, are discretized at the cell centres. A standard second-order central-difference scheme is used to discretize all the spatial derivatives at the nodes located in the bulk flow region. The unsteady equation are marched in time using a variation of Chorin's projection–correction approach, and the Crank–Nicolson scheme is used to discretize all the terms in the momentum equation in its conservative form. The fluid–solid interface is represented by a set of Lagrangian marker points and 3-node triangular elements. To implement the boundary conditions at the interface, 'ghost nodes' outside the fluid region are defined at each time step, at which the flow variables are extrapolated (Mittal *et al.* 2008). To suppress the numerical oscillations that may happen when solving a moving-boundary problem, 'hybrid nodes' are defined inside the fluid region, at which the flow variables are weighted averages between the interpolated solution and the solution to the Navier–Stokes equations.

The structural solver is the finite-element package for solid mechanics, NonStaD (standing for nonlinear analysis of statics and dynamics), developed by Professor Doyle at Purdue University. NonStaD is designed specially for thin-walled structures consisting of frames, membranes, plates, and shells. The software has the capability of handling large displacements and large rotations, and the constitutive laws include both elasticity and plasticity. A description of the numerical approach used in NonStaD and instructions for the software usage are provided in several publications (Doyle 1991, 2001, 2008). The 3-node triangular element in the approach supports both in-plane (membrane) and out-of-plane (flexural) deformations. Each node has six global degrees of freedom (DoF), including three displacement components and three angles of rotation. The plate element used is the discrete Kirchhoff triangular (DKT) element, which has been widely researched and documented as being one of the most efficient

https://doi.org/10.1017/jfm.2011.543 Published online by Cambridge University Press

flexural elements (Batoz, Bathe & Ho 1980). The large-displacement and small-strain deformation in the structural solver is handled using the corotational scheme. That is, a local coordinate system is envisioned as moving with each discrete element, and relative to this coordinate system, the element behaves linearly as described by the Kirchhoff–Love theory of plates. Consequently, the nonlinearities of the problem are results of the coordinate transformation. The time stepping of the equation is achieved using an incremental/iterative strategy.

The incompressible Navier–Stokes equations are combined with the structural dynamics through the boundary conditions, which include the no-slip, no-penetration, and traction conditions. The flow and structural solvers share the triangular mesh on the wetted surface of the solid, and the pressure and viscous stress are interpolated onto the nodal points of the surface mesh. To achieve the implicit coupling for the fluid–structure interaction, we solve the flow and structure in an iterative manner.

3.2. *Code validation*

In addition to the validation tests described in our previous publications for the current numerical method, two other tests are performed here for problems pertinent to flapping wings. The first problem concerns an impulsive flow over a rigid rectangular plate, which was studied numerically by Taira & Colonius (2009). The stationary plate has a rectangular shape and has an aspect ratio of 2. The angle of attack of the plate is fixed at 40°, and the Reynolds number based on the free-stream velocity U and the chord length c is $Re = 500$. The 3D simulation is done in a $10c \times 10c \times 6c$ (in the streamwise, transverse, and spanwise directions) domain and on a $211 \times 121 \times 141$ grid. In figure 2 we present the wake development by showing the isosurface of the vorticity magnitude equal to $5U/c$ at different time instants in a top view. The corresponding flow field from Taira & Colonius (2009) is shown for comparison. It can be seen that the instantaneous vortex structures from the two simulations agree with each other very well.

The second validation test is a moving-boundary problem. We simulate the flow around two robotic fruit fly wings, replicating the experiment in Dickinson *et al.* (1999). The wings are models of *Drosophila melanogaster* and have a span of $R = 0.25$ m. The area of each wing is $S = 0.0167$ m^2 and the average chord is $\bar{c} = 8.79$ cm. The wing shape used is similar to the one reproduced in Bai, Cui & Zhan (2009). In the experiment of Dickinson *et al.* (1999), one flapping period is composed of two half-strokes and the flapping frequency is $f = 0.145$ Hz. The wings sweep in the horizontal plane and rotate at the end of each stroke. The wing rotation occurs symmetrically with respect to the stroke reversal and lasts 16 % of the flapping period. The stroke amplitude is 160°, and the angle of attack at mid-stroke is 40°. The Reynolds number is $Re = U\bar{c}/\nu = 164$, where $U = 0.215$ m s^{-1} is the average translational velocity at the wing tip and $\nu = 115$ cSt is the kinematic viscosity of the fluid.

A non-uniform Cartesian grid of size $251 \times 251 \times 181$ is used, which provides clustered points around the wings. The size of the computational domain is equivalent to that of the oil tank in the experiment. Dirichlet boundary conditions for the velocity are imposed on the sidewalls, and open boundary conditions are imposed on the top and bottom boundaries. The simulation is conducted for five flapping cycles. The temporal variation of the lift coefficient during each stroke is virtually identical after the third cycle. Figure 3 shows the time history of the lift coefficient from the fourth cycle for the case with symmetrical rotation, together with the experimental Dickinson *et al.* (1999) and two numerical results (Sun & Tang 2002; Kweon & Choi 2010). As

https://doi.org/10.1017/jfm.2011.543 Published online by Cambridge University Press

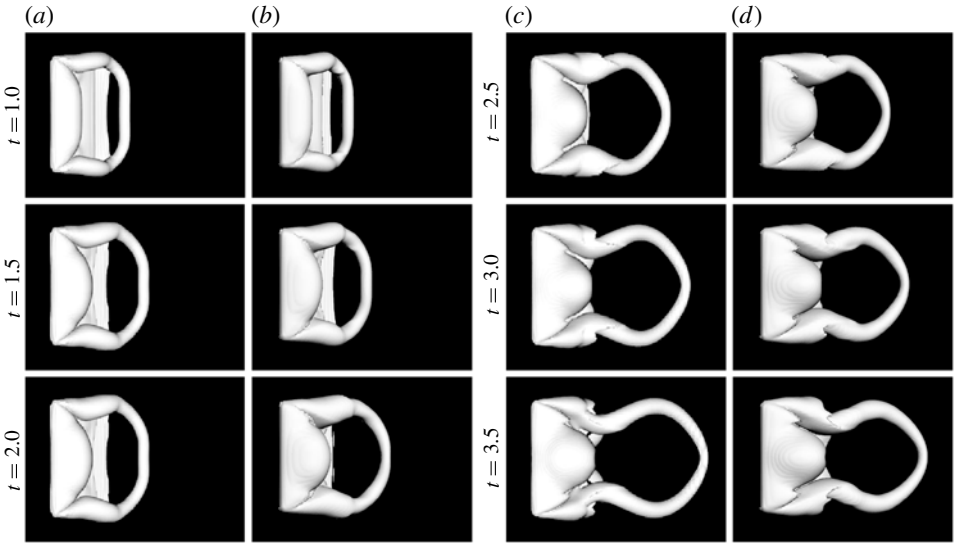


FIGURE 2. Top view of wake development behind a stationary rectangular plate at an angle of attack of 40°. Columns (*a*) and (*c*) are from Taira & Colonius (2009), and columns (*b*) and (*d*) from the current simulation. The time is normalized by c/U.

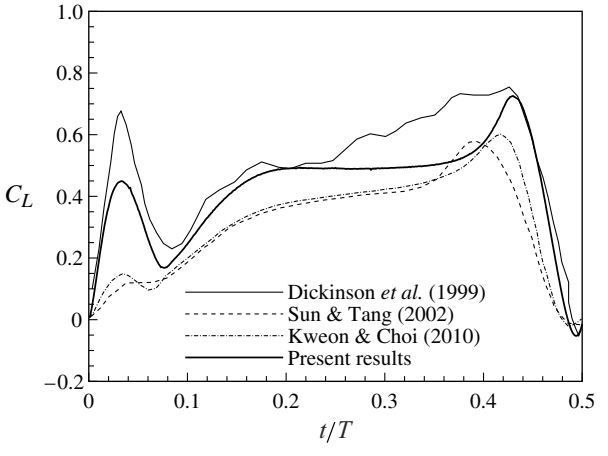


FIGURE 3. Instantaneous lift coefficient, $C_L = 2F_L/(\rho U^2 S)$, for a robotic fly.

we can see, our simulation captures the two lift peaks produced near the beginning and end of the half-stroke. Furthermore, our result compares better with the experimental data than the other two numerical results. It should be stressed that the numerical results from Sun & Tang (2002) and Kweon & Choi (2010) were obtained from simulations of only one single wing, while both the current simulation and the experiment have a pair of wings.

3.3. *Grid and domain convergence*

The rectangular domain used in the current study has a size of $14c \times 15c \times 15c$. This choice of domain size is based on our experience and also previous work on similar

https://doi.org/10.1017/jfm.2011.543 Published online by Cambridge University Press

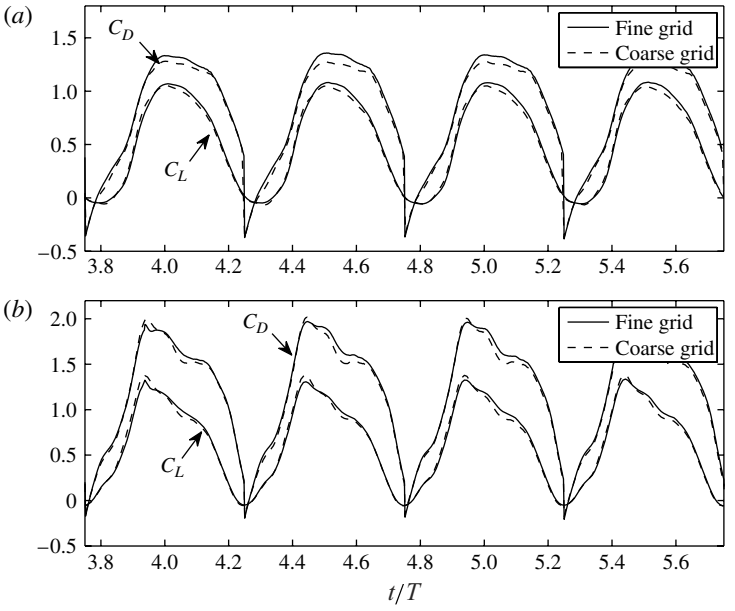


FIGURE 4. Lift and drag histories computed on the coarse grid (1.7M points) and fine grid (7.8M points) for $m^* = 1$ (*a*) and $m^* = 5$ (*b*), $\omega^* = 0.36$, $\varphi = 0$, and $Re = 176$.

topics. For example, a domain of $15c \times 15c \times 16c$ was used by Dong, Mittal & Najjar (2006) for their simulation of an elliptical pitching/heaving foil of aspect ratio 2. The typical grid used in this study has $140 \times 116 \times 106$ (or 1.7M) mesh points, and the smallest grid spacing is $0.05c$ around the wing in all three directions. To verify that this grid resolution is sufficient, we use a $240 \times 196 \times 166$ (or 7.8M points) mesh and double the resolution around the wing in all three directions. Figure 4 shows the time-varying lift and drag coefficients for two mass ratios $m^* = 1$ and 5, $\omega^* = 0.36$, $\varphi = 0$, and $Re = 176$. The force histories only show small differences between the fine and coarse resolutions. We further compute the time-averaged lift, drag, and power coefficients and their ratios from both simulations. The results are listed in table 1, from which we can see that the relative differences are all below 5 %. Thus, the resolution used in the present simulation is deemed satisfactory. The time step size here is $\Delta t = 0.002T$, where T is the period of a complete cycle. For a typical simulation, one stroke cycle takes around 14 h of wall time on 16 AMD Opteron® processor cores running at 2.3 GHz.

4. Results and analysis

In this section, we present the simulation results for mass ratios $m^* = 0.5$, 1 and 5, and frequency ratios $\omega^* = 0, 0.11, 0.25, 0.30, 0.36$ and 0.51. Note that $\omega^* = 0$ corresponds to the rigid wing. The specific values of ω^* are arbitrarily set to span the range of rigidity under consideration. We will first present the results and analysis for the case of symmetric pitching, $\varphi = 0$, in §§ 4.1 and 4.2, and then present the asymmetric pitching cases in § 4.3. The Reynolds number in these simulations is $Re = 176$. The flow field and the effect of the Reynolds number will be provided in §§ 4.4 and 4.5, respectively.

https://doi.org/10.1017/jfm.2011.543 Published online by Cambridge University Press

Mass ratio	Grid	C_L	C_D	C_P	C_L/C_D	C_L/C_P
	7.8M Grid	0.536	0.832	0.776	0.664	0.691
$m^* = 1$	1.7M Grid	0.523	0.794	0.748	0.658	0.699
	Difference	3 %	5 %	4 %	2 %	1 %
	7.8M Grid	0.661	1.226	1.067	0.539	0.619
$m^* = 5$	1.7M Grid	0.652	1.193	1.048	0.547	0.622
	Difference	1 %	3 %	2 %	2 %	1 %

TABLE 1. Grid-convergence study for $m^* = 1$ and 5, $\omega^* = 0.36$, $\varphi = 0$, and $Re = 176$.

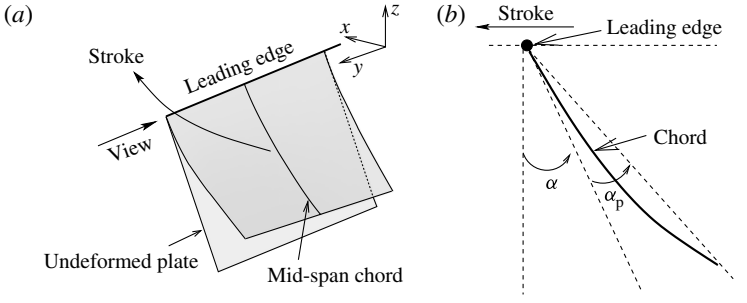


FIGURE 5. Illustrations of (*a*) the deformed wing and chord and (*b*) definition of the passive pitching angle, α_p.

A notable difference between the current 3D simulation and the previous 2D simulations (Vanella *et al.* 2009; Eldredge *et al.* 2010; Yin & Luo 2010) is that the present 3D flow and wing vibration quickly develop into a nearly periodic state after about two cycles and they also become symmetric between two half-strokes. In the 2D simulations, both the wing deformation and flow may exhibit significant asymmetry and also cycle-to-cycle variations even after the flow is established. As shown by Eldredge *et al.* (2010) and Yin & Luo (2010), these phenomena are caused by the irregularities in the vortex shedding and wing–vortex interaction. Such variable behaviours are not obvious in our 3D simulations. The possible reason is that in 3D, the tip vortex stabilizes the leading-edge vortex and thus has prevented it from shedding (Ellington *et al.* 1996).

4.1. *Wing deformation*

In the present model, the leading edge is stiff, so its twisting and bending deformations can be ignored. In all the flexible plate cases, the wing deformation is dominated by the typical chordwise bending illustrated in figure 5. Since the bending is greater at the wing tip than at the root due to the non-uniform load along the span, the entire wing surface is also warped. To quantify the amount of chordwise deformation, and for the later discussion of its effect on the aerodynamic forces, we define the local passive pitching angle, α_p, as the included angle between the deformed wing and its equilibrium position, measured in a plane perpendicular to the leading edge (see figure 5). The effective pitching angle, α_e, is then given by $\alpha_e = \alpha + \alpha_p$.

The instantaneous wing deformation at different phases of a stroke is visualized in figure 6 for $m^* = 0.5$, 5 and $\omega^* = 0.36$. In this figure, the wing shape is viewed from

https://doi.org/10.1017/jfm.2011.543 Published online by Cambridge University Press

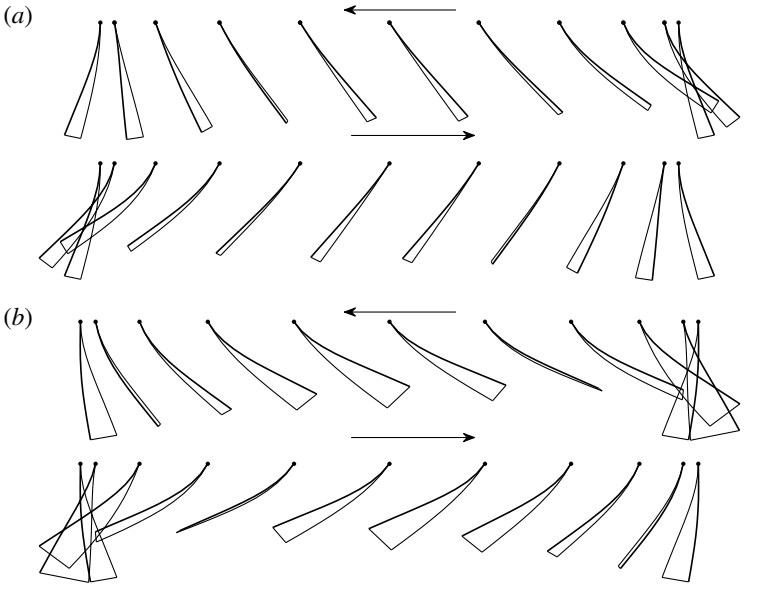


FIGURE 6. Wing deformation in one flapping cycle as viewed by following the leading edge and from the wing tip, where the thick line is the tip edge and the thin line is the base edge. (*a*) $m^* = 5$ and (*b*) $m^* = 0.5$, $\omega^* = 0.36$, and $\varphi = 0$.

the tip to the base (indicated in figure 5*a*) with the upward vector of the camera unchanged. In addition to the chordwise deformation, a spanwise deformation can be seen in figure 6 from the instantaneous shapes of the chords at the two ends of the wing. For $m^* = 5$, significant surface warping is observed during wing reversal when the wing experiences the greatest acceleration, and only small spanwise deformation is seen during mid-stroke. For $m^* = 0.5$, large spanwise deformation is observed during both wing reversal and mid-stroke, and its magnitude is much higher than that in the case of $m^* = 5$, especially during wing reversal. Despite the significant difference in the surface warping, the magnitudes of chordwise deformation as measured at mid-span are still comparable between these two cases, which will be shown later. In both cases, the spanwise twist disappears somewhere between the wing reversal and mid-stroke, where the chords at the tip and base are temporarily aligned. The phase difference among the chords causes the deformation to appear to propagate from the wing tip to the base as a long spanwise wave.

To demonstrate a typical wing behaviour, the active pitching angle, passive pitching angle, and effective pitching angle at mid-span for $m^* = 5$ and $\omega^* = 0.36$ are shown in figure 7(*a*) for an established cycle. It can be seen that α_p is overall in phase with α, meaning the chord bends backward, i.e. in the opposite direction to the stroke. However, the magnitude of α_p exhibits two distinct peaks during each half-cycle (the peaks are negative for the second half-cycle, $t/T = 0.5$ to 1): one taking place during the wing-acceleration stage and the other during the wing-deceleration stage. Here the wing acceleration and deceleration refer to the translational motion of the chord due to the stroke rotation of the entire wing. Between the two peaks, there is a valley where α_p is reduced in magnitude but still has the same sign as α so that the effective pitching is greater than the active pitching. The temporal characteristics of the passive pitching angle can be explained by the combination of the wing inertia, the

https://doi.org/10.1017/jfm.2011.543 Published online by Cambridge University Press

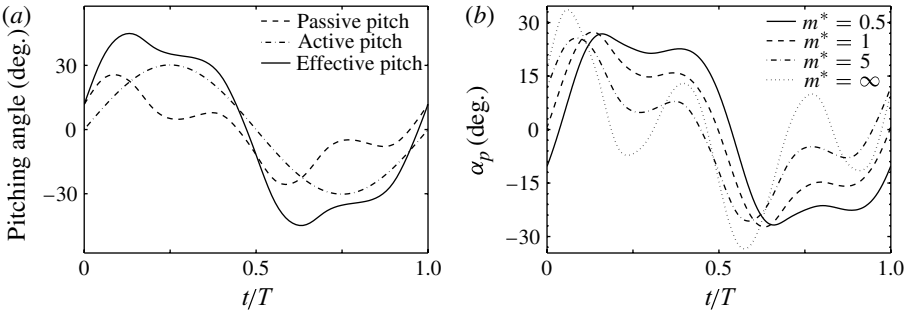


FIGURE 7. (*a*) Active, passive, and effective pitching angles at mid-span in a cycle for $m^* = 5$. (*b*) Passive pitching angle at mid-span for different mass ratios. $\omega^* = 0.36$ and $\varphi = 0$.

aerodynamic drag and lift, and the elastic force at different phases of a single stroke. During the acceleration stage of a stroke, the inertial force of the wing is high, and the aerodynamic forces are rising. The two effects work collaboratively to deform the wing until α_p reaches its highest degree. Before the wing chord reaches mid-stroke and its maximum translational speed, the inertial force drops, and the wing starts its elastic rebound against the aerodynamic forces. Note that the natural frequency of the wing is almost three times the flapping frequency in this case. As a result, α_p starts to drop but still has the same sign as α since the drag and lift are high at this moment. After the wing passes the mid-stroke and starts to decelerate, the natural oscillation works together with the aerodynamic forces, causing the chord to bend again and thus α_p to increase for the second time. However, the second peak is much smaller than the first one. Prior to the end of the half-stroke at $t/T = 0.5$, the aerodynamic forces drop and the inertial force, now with an opposite sign due to deceleration of the wing, is growing in strength. Thus, the chord deforms in the other way, and α_p becomes negative.

It should be pointed out that the two-peak oscillations in the pitching angle are also observed in real insect wings (see figure 4 in Walker, Thomas & Taylor 2010). In the present case, the first peak is caused by the inertia force and the second one has a significant contribution from the flow. As seen from the plot of α_e in figure 7(*a*), the temporal behaviour of the passive pitching causes the total pitching angle to deviate from the active pitching significantly. Such deviation has an important effect on the lift and drag forces and will be discussed later in § 4.2.

To see the effect of the wing inertia on the chordwise deformation, we plot the passive pitching angle at mid-span in figure 7(*b*) for mass ratios $m^* = 0.5$, 1, 5, and ∞ (i.e. the 'in-vacuum' case). The frequency ratio is again $\omega^* = 0.36$. For all the cases, it can be seen that α_p has two peaks within each half-cycle. However, the two peaks are more visible as m^* is increased, indicating that the natural vibration of the wing becomes more significant at higher mass ratios. The natural vibration is most obvious for the $m^* = \infty$ case, where the aerodynamic forces are absent. In fact, since there is no external damping in this case, the wing deformation is significantly aperiodic, with the phases of the two peaks relatively consistent but the magnitudes varying randomly from cycle to cycle by approximately 30 %. On the other hand, for the lowest mass ratio, $m^* = 0.5$, the two peaks are much less clear, indicating that the wing deformation is sustained by the aerodynamic forces during mid-stroke.

https://doi.org/10.1017/jfm.2011.543 Published online by Cambridge University Press

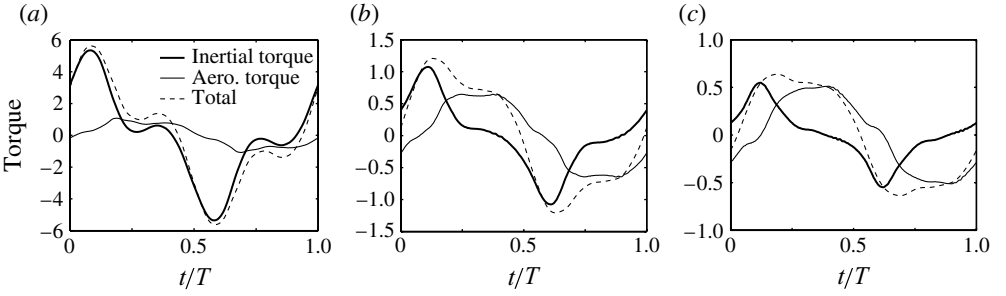


FIGURE 8. Instantaneous inertial and aerodynamic torques around the leading edge reduced by $(1/2)\rho U^2c^2L$ for (*a*) $m^* = 5$, (*b*) $m^* = 1$, and (*c*) $m^* = 0.5$ where $\omega^* = 0.36$ and $\varphi = 0$.

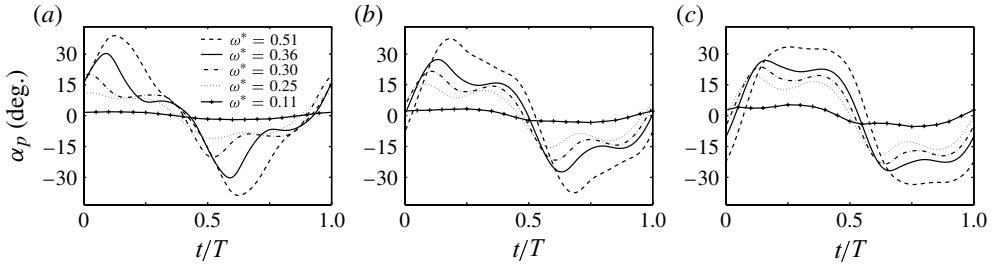


FIGURE 9. Passive pitch angle at mid-span in one cycle for cases of various frequency ratios for (*a*) $m^* = 5$, (*b*) $m^* = 1$ and (*c*) $m^* = 0.5$.

Another observation from figure 7(*b*) is that the first peak for $m^* = 0.5$, 1 and 5 has a similar magnitude with $\alpha_p \approx 26°$, while the second peak varies from $\alpha_p = 8°$ to $\alpha_p = 23°$. The similar amount of wing deformation at different mass ratios will allow us to concentrate on the history of the deformation rather than the magnitude when we compare the aerodynamic performance of these cases.

To better understand the temporal behaviour of the wing deformation, we calculate both the inertial torque and the aerodynamic torque around the leading edge. The results are shown in figure 8 for the cases of $m^* = 0.5$, 1, and 5. These cases correspond to those in figure 7(*b*). Here the torques are normalized by $(1/2)\rho U^2c^2L$. For $m^* = 5$, the maximum inertial torque takes place soon after the start of the stroke or somewhere before one-quarter of the half-cycle. In comparison, the aerodynamic torque is much lower and is only comparable to the second peak of the inertial torque. As the mass ratio is reduced, the aerodynamic torque becomes more important relative to the inertial torque. For $m^* = 1$, the peak aerodynamic torque reaches more than 50 % of the peak inertial torque, and for $m^* = 0.5$, the two torques have a comparable magnitude. In all three cases, the aerodynamic torque reaches its maximum level well after the inertial torque and has a much longer duration. In addition to the relative magnitude, the histories of both the inertial and aerodynamic torques at the low mass ratios are also different from those at the high mass ratio, which can be regarded a signature of the two-way fluid–structure interaction. In the cases of $m^* = 1$ and 0.5, the second peak of the inertial torque has disappeared due to the increased fluid damping. Furthermore, as the mass ratio is reduced, the aerodynamic torque has a lower magnitude and a larger portion of this torque has an opposite sign in the beginning of the half-stroke.

https://doi.org/10.1017/jfm.2011.543 Published online by Cambridge University Press

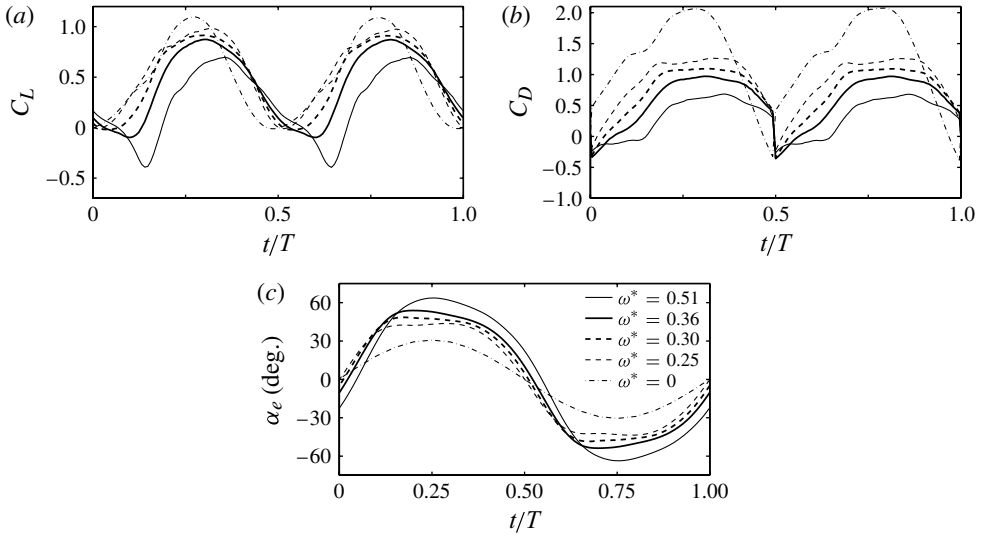


FIGURE 10. Lift (*a*), drag (*b*), and effective pitch (*c*) histories for $m^* = 0.5$ and $\varphi = 0$. Note that the jump in C_D during wing reversal is due to the present definition of the drag.

From the torque plots, it is straightforward to explain the behaviour of the passive pitching in figure 7(*b*). At mass ratio $m^* = 0.5$, the total torque is relatively constant during much of the half-stroke and has produced a similar pattern in the passive pitching angle. In addition, the opposite aerodynamic torque before and during stroke reversal works against the inertial torque for the low mass ratios, and thus the pitching rotation of the wing is delayed for $m^* = 0.5$ and 1.

The effect of wing rigidity on the passive pitching angle at mid-span is shown in figure 9 for mass ratios $m^* = 0.5$, 1, and 5. For all the mass ratios, the maximum value of the passive pitching angle increases as the frequency ratio ω^* is raised. This value varies between 11.5° and 38° for $m^* = 5$ as ω^* goes from 0.25 to 0.51. The range of variation decreases for lower mass ratios and is between 15.5° and 37° for $m^* = 1$ and between 19° to 33° for $m^* = 0.5$. The figure also shows that in the most flexible case, $\omega^* = 0.51$, the two-peak pattern of α_p disappears and is replaced by a much wider single peak for all three mass ratios. For the high mass ratio at $m^* = 5$, this change is because the forced vibration becomes close to the natural vibration of the wing structure. For low mass ratios such as $m^* = 0.5$, the single peak of α_p at $\omega^* = 0.51$ has a nearly flat top and is apparently caused by the prolonged aerodynamic effect. Finally, in the cases of low mass ratios and high frequency ratios (e.g. $m^* = 0.5$ and $\omega^* = 0.51$), α_p has an opposite sign in the beginning of a half-stroke compared to the rest of the half-stroke. That is, α_p is negative at $t/T = 0$ and positive at $t/T = 0.5$, which means that the wing rotation at stroke reversal is delayed. The situation is opposite for high mass ratios. In the case of $m^* = 5$, α_p typically has the same sign between the start and rest of the half-stroke, i.e. positive at $t/T = 0$ and negative at $t/T = 0.5$. The result means that the wing rotation at stroke reversal is advanced.

4.2. *Lift, drag, and aerodynamic power*

To study the consequence of the dynamic deformation, we compute instantaneous lift, drag, and aerodynamic power consumed by the wing. The characteristics of these variables are found to be closely associated with the temporal behaviour of the

https://doi.org/10.1017/jfm.2011.543 Published online by Cambridge University Press

wing deformation. We will first show the instantaneous forces for each mass ratio and discuss the relationship between the forces and wing deformation. Then we will combine the stroke-averaged data and discuss the overall effect of the wing flexibility and mass ratio.

The instantaneous lift and drag coefficients for $m^* = 0.5$ are shown in figure 10(*a,b*) at $\omega^* = 0$ (rigid wing), 0.25, 0.30, 0.36, and 0.51. The corresponding effective pitching angle, α_e, is plotted in figure 10(*c*) to facilitate discussion. In figure 10(*a*), all lift graphs display a single peak around or after the mid-stroke. As ω^* is increased and thus the wing becomes more flexible, the peak lift is reduced. There are two possible reasons for this reduction. First, the effective angle of attack, defined as the angle between the straight line connecting leading and trailing edges of a chord and the direction of the stroke, is lower as the wing deforms more. According to Dickinson *et al.* (1999), the optimal angle of attack is around 45° for a rigid uncambered wing. The lowest angle of attack in the present case is near 25° for the most flexible case. Second, the deformed chord forms a reverse camber, as seen in figure 6, and is thus not beneficial for lift production. For the latter, some structural features of real insect wings, such as allowing the leading edge to twist or having a pre-existing camber (Ennos 1988*a*), would help alleviate the problem. Comparing the validation study described in § 3.2 for the robotic wing (see figure 3), the lift graphs in the present simulations display only one single peak during a half-cycle. This is because in the validation problem, the wing has a relatively constant angle of attack during much of stroke but undergoes quick pitching rotation during stroke reversal, while in the present study the active pitching motion is simply sinusoidal.

Although the peak lift is reduced for the flexible cases as shown in figure 10(*a*), the average lift may not be. Since the effective angle of attack for this low mass ratio is sustained by the aerodynamic torque during wing translation as seen in figure 10(*c*) (in the present definition, the effective angle of attack is complementary to the effective pitching angle α_e), the flexible wings, though not necessarily at an optimal position, may still produce significant lift after mid-stroke.

Figure 10(*b*) shows that as the wing becomes more flexible, the drag decreases significantly. This is mainly because the frontal area of the wing is reduced due to the chordwise deformation. For the most flexible wing, i.e. $\omega^* = 0.51$ in figure 10(*a*), the lift may be adversely affected. This result was also found in previous studies (Eldredge *et al.* 2010; Yin & Luo 2010). In the current case, the lift graph for $\omega^* = 0.51$ contains a large portion of negative value. This lift loss is due to the much delayed wing rotation during stroke reversal, as seen from figure 10(*c*). The effective pitching long after stroke reversal causes the trailing edge to move upward while the wing is accelerating, thus generating a downward force. Note that in figure 10(*b*), the delayed wing rotation also leads to a negative drag (or a thrust). The result is understandable since the recovering motion of the trailing edge is in the opposite direction to the wing translation and thus functions as a temporary propulsor.

Figure 11 shows the lift, drag, and effective pitching histories for $m^* = 5$ and ω^* from 0 to 0.51. Contrary to the low-mass-ratio case of $m^* = 0.5$, for $m^* = 5$ the peak lift becomes higher when ω^* is increased. Furthermore, the timing of the peak lift does not appear to have a consistent trend. Instead, the lift may peak either before, near, or after the mid-stroke. To explain this phenomenon, we shall again look at the characteristics of wing deformation. For the wing at $\omega^* = 0.36$, the passive pitching angle history in figure 7(*a*) shows that α_p has a sharp drop after the first peak, which suggests that the wing is recovering its shape due to elastic rebound. Such a quick recovery counteracts the active pitching and leads a sudden drop in the effective

https://doi.org/10.1017/jfm.2011.543 Published online by Cambridge University Press

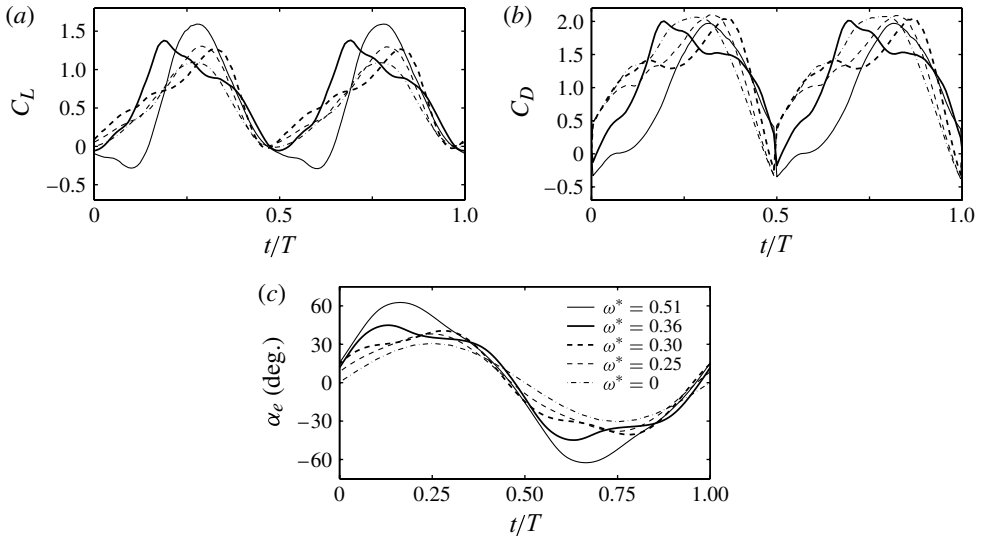


FIGURE 11. Lift (*a*), drag (*b*), and effective pitch (*c*) histories for $m^* = 5$ and $\varphi = 0$.

pitching angle prior to mid-stroke as seen in figure 11(*c*). Thus, the trailing edge of the wing presses downward and produces extra lift, causing the total lift to peak before mid-stroke. This effect is not obvious for $m^* = 0.5$ where the aerodynamic forces act as a strong damping source delaying the wing recovery.

For $m^* = 5$ and $\omega^* = 0.30$, the situation is slightly different. In this case, the effective pitching is highest after mid-stroke when the elastic recovering and the active pitching are in the same direction. As a result, the extra lift caused by the wing rotation leads to a delayed lift peak.

The drag histories plotted in figure 11(*b*) show that the drag produced by the flexible wing is comparable to that by the rigid wing. This result is in sharp contrast with that for $m^* = 0.5$. In addition, the drag at $m^* = 5$ may oscillate during a half-cycle. To understand these phenomena, we notice that the elastic recovery of the wing may take place when the wing is translating fast and the recovery may happen twice in a half-cycle. In addition, the elastic recovery not only increases the frontal area of the wing but also causes the wing to move faster relative to the fluid. As a result, the drag force is significantly increased during wing translation.

From the histories of the aerodynamic forces and wing deformation, we see that the lift and drag of a flexible wing depends not only on the instantaneous pitching angle but also on the rate of pitch and camber of the wing. To compare the overall performance of the wings, we compute the mean force and power coefficients for all the cases. The averaged data are taken over several established cycles. The results are shown in figure 12, from which we may see clearly the effect of wing flexibility and inertia.

We first look at the mean lift coefficient plotted against the frequency ratio in figure 12(*a*) for the three mass ratios, $m^* = 0.5$, 1, and 5. Here the rigid wing is represented by the case $\omega^* = 0$, at which the wing inertia has no effect on the aerodynamics since the wing kinematics has been prescribed. For each mass ratio, we see that moderate wing flexibility increases the lift, but excessive flexibility may not help with lift production and even leads to lift loss. As discussed earlier, the lift augmentation mechanisms for different mass ratios are not entirely the same. At high

https://doi.org/10.1017/jfm.2011.543 Published online by Cambridge University Press

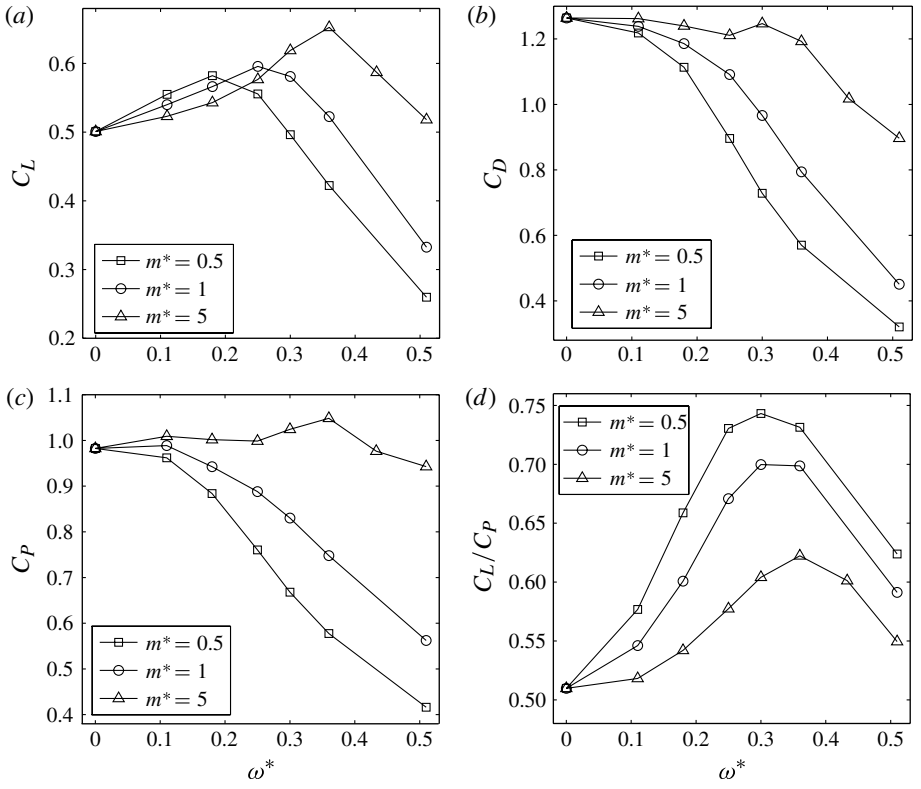


FIGURE 12. Mean lift (*a*), drag (*b*) and power (*c*) coefficients, and lift-to-power ratio (*d*) for the three mass ratios and $\varphi = 0$.

mass ratios, the lift enhancement is due to the passive rotation of the wing during elastic recovery, while at low mass ratios, the enhancement is more likely to be due to a combination of wing recovery and the prolonged favourable angle of attack during a stroke. Similar to the 2D study by Yin & Luo (2010), there exists an optimal ω^* at which the highest lift is produced, and this optimal point moves to a higher value as the mass ratio is raised. Figure 12(*a*) shows that the optimal ω^* is around 0.2, 0.25, and 0.35 for the mass ratio $m^* = 0.5$, 1, and 5, respectively. Furthermore, the figure shows that the maximum lift is higher for the wing with larger mass ratios. This maximum value is $\bar{C}_L = 0.55$ for $m^* = 0.5$ and $\bar{C}_L = 0.65$ for $m^* = 5$.

Figure 12(*b*) shows the mean drag coefficient for the three mass ratios and a range of wing flexibility. The overall trend is that the drag drops when the wing flexibility is increased. At the highest mass ratio, $m^* = 5$, the drag is only slightly lower than that of the rigid wing for most of the cases except for $\omega^* = 0.51$, where the drag is also significantly reduced. The lowest mass ratio, $m^* = 0.5$, has the lowest drag among the three mass ratios, which is understandable since the wing yields to the aerodynamic torque during wing translation and on average it has the least frontal area and the lowest rate of pitch. This result is consistent to the 2D study in Yin & Luo (2010).

By prescribing the stroke and pitching motions at the wing root, the wing receives input energy from the driving force at the root. The energy then is passed into the surrounding fluid through the aerodynamic forces. The elastic wing serves as an energy capacitor by temporarily storing energy in the forms of elastic potential and

https://doi.org/10.1017/jfm.2011.543 Published online by Cambridge University Press

later releasing it in the forms of kinetic energy and work output done on the fluid. Thus, there is energy reception and delivery accompanying the wing deformation and recovery. Even though the elastic wing does not consume energy itself (if internal damping is not considered), a wing with different stiffness and mass may require different levels of energy input at a particular time moment. Furthermore, the energy delivery to the fluid is through both lift and drag, and the former would lead to a higher efficiency. In figure 12(*c,d*) we plot the mean power coefficient and the aerodynamic efficiency. Unlike the 2D study of Yin & Luo (2010), here we exclude the inertial power and evaluate the power efficiency by calculating the net aerodynamic power only. In Yin & Luo (2010), the power calculation was based on the input from the wing root, and the negative power was not taken into account when calculating the ratio between the lift and the net power. Their treatment was based on a conservative assumption that insects may not have a mechanism to make use of the negative power. In the present study, such a treatment is not adopted because it would exclude the negative inertial power and is thus inappropriate for the wing with a high mass ratio and large input power oscillations (note that regardless of the power treatment, the main conclusions from Yin & Luo 2010 would remain the same because they could be drawn alternatively from the lift-to-drag ratio).

The power coefficient in figure 12(*c*) displays a similar trend as the drag coefficient as ω^* and m^* are varied. This is because most of the energy has been consumed through the drag rather than through the lift. For $m^* = 5$ the power coefficient does not change significantly as ω^* is varied. For the other two mass ratios, the power coefficient drops quickly as ω^* is increased. The efficiency plotted in figure 12(*d*) clearly shows the advantage of the wings with moderate flexibility. The optimal flexibility for all three mass ratios is around $\omega^* = 0.3$ to 0.35, where the peak efficiency is about $C_L/C_P = 0.62$ for $m^* = 5$, 0.70 for $m^* = 1$, and 0.74 for $m^* = 0.5$. These values are significantly higher than the efficiency in the rigid case, which has $C_L/C_P = 0.51$. At all frequency ratios except $\omega^* = 0$, the lift efficiency is increased as m^* is reduced. This result can be explained by the very low drag generated by the wing with a low mass ratio.

4.3. *Advanced and delayed pitching*

We have seen that in the present simulation, the chordwise flexibility increases the effective pitching angle of the wing. In addition, a high mass ratio leads to an advanced pitching motion with respect to the wing stroke, while a low mass ratio leads to a delayed pitching. Furthermore, we have shown that the timing of the passive pitching has an important effect on aerodynamic forces and power efficiency of the wing. These observations motivate us to vary the phase of the active pitching and then see if the wing deformation still has a similar effect, i.e. causing the pitching motion to be further advanced or delayed. This study is done by setting the phase angle in (2.2) to $\varphi = \pi/4$ for advanced pitching or $\varphi = -\pi/4$ for delayed pitching, which are typical values used in previous wing models (Wang, Birch & Dickinson 2004; Eldredge *et al.* 2010). The results shall be compared with those for symmetric pitching with $\varphi = 0$.

Figure 13(*a,b*) shows instantaneous deformation of the wing chord measured at mid-span for delayed pitching. Cases with mass ratio $m^* = 0.5$ and 5 and frequency ratio $\omega^* = 0.51$ have been shown here. The corresponding effective pitching angle and lift coefficient are plotted in figure 13(*c,d*). Comparing the flexible case with the rigid case, both with the same active pitching, we notice that during the entire stroke, $m^* = 5$ causes a phase advance in effective pitching with respect to the delayed active

https://doi.org/10.1017/jfm.2011.543 Published online by Cambridge University Press

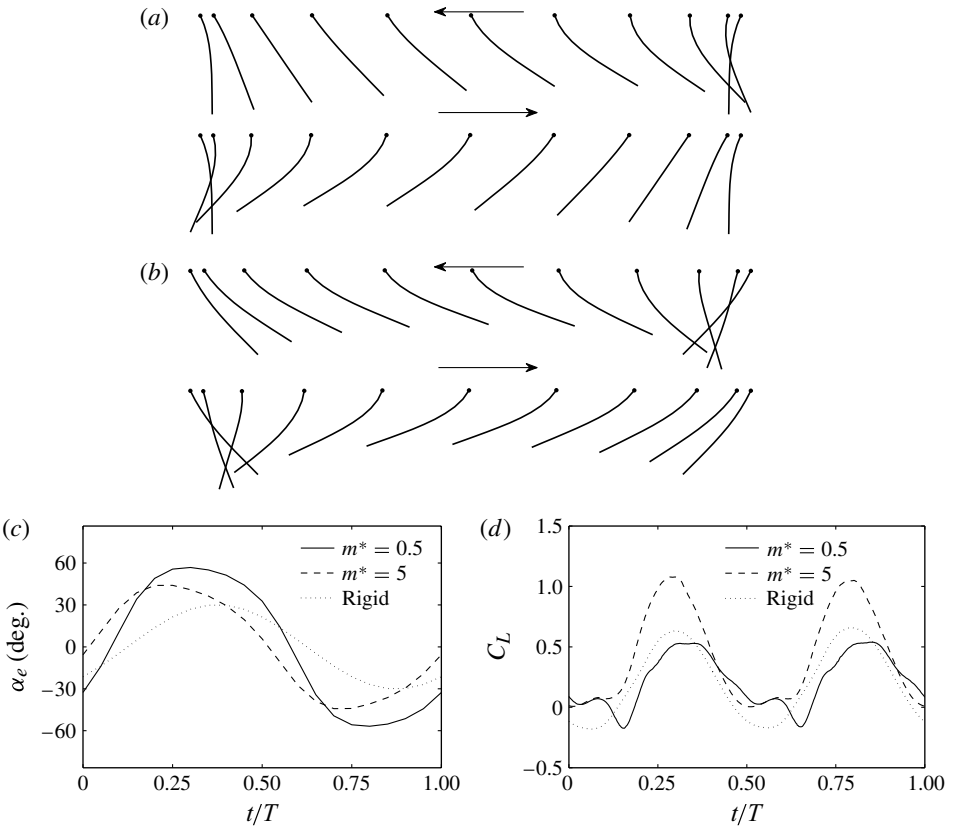


FIGURE 13. (*a*,*b*) Chord deformation at mid-span, (*c*) effective pitching angle, and (*d*) lift coefficient in delayed pitching with $\omega^* = 0.51$, $\varphi = -\pi/4$, and (*a*) $m^* = 5$, (*b*) $m^* = 0.5$.

pitching. As a result of this phase compensation, the effective pitching at $m^* = 5$ is more or less like to a rigid wing performing symmetric pitching. In this case, the effect of the mass ratio on the wing deformation is thus consistent with that in the symmetric pitching case. The situation, however, is different for $m^* = 0.5$. From figure 13(*b*,*c*), the wing at this low mass ratio does show a further pitching delay with respect to the already delayed active pitching during stroke reversal, i.e. at $t/T = 0$ and 0.5, but the maximum effective pitching is still advanced compared to the active pitching and takes place around mid-stroke. Apparently, the dynamic pitching in this case is modified by the aerodynamic forces.

The instantaneous lift coefficient in figure 13(*d*) shows that the rigid and $m^* = 0.5$ cases both contain a significant portion with negative lift during early stage of a half-stroke, while the $m^* = 5$ case has a positive lift during an entire stroke. For the rigid case, the negative lift is due to the reverse angle of attack. For $m^* = 0.5$, the reverse angle of attack in the beginning of the stroke ($t/T = 0$) does not lead to a negative lift. This is because, as intuitively seen in figure 13(*b*), the effect of the reverse angle of attack is compensated by the rate of pitch that is positive at this moment under the collaborative effects of the active pitching, inertial torque, and elastic recovery. However, the lift for $m^* = 0.5$ becomes negative at a later time during wing acceleration, which is due to the high positive rate of the effective pitch at that

https://doi.org/10.1017/jfm.2011.543 Published online by Cambridge University Press

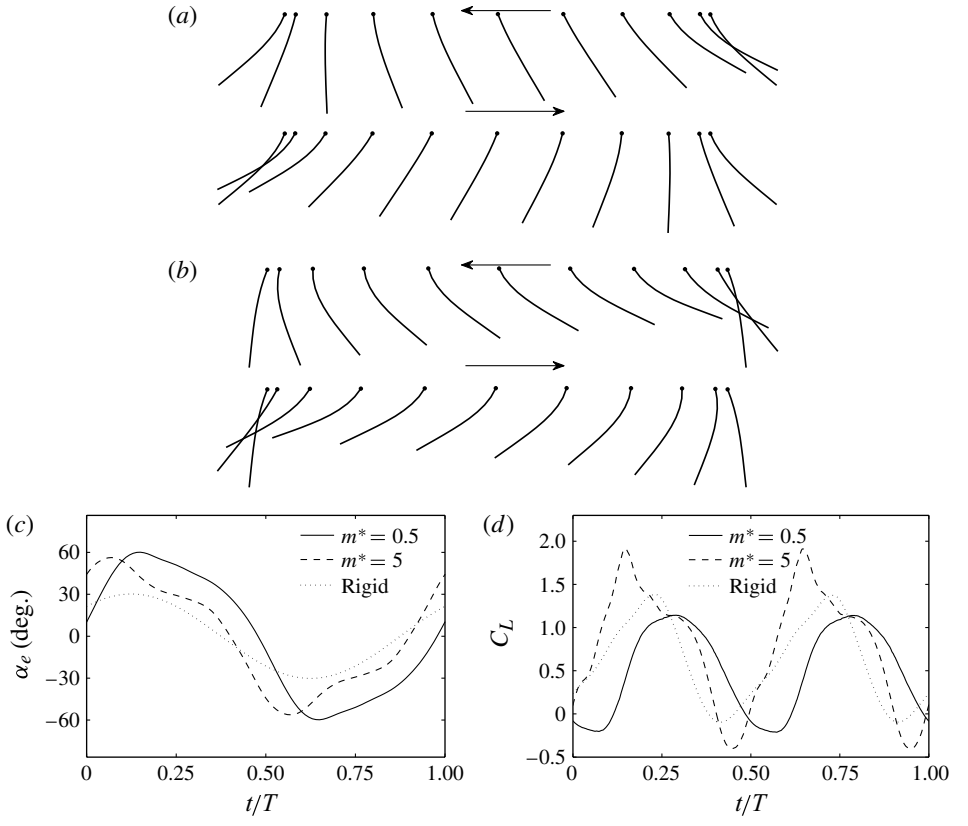


FIGURE 14. (*a*,*b*) Chord deformation at mid-span, (*c*) effective pitching angle, and (*d*) lift coefficient in advanced pitching with $\omega^* = 0.36$, $\varphi = \pi/4$: and (*a*) $m^* = 5$; (*b*) $m^* = 0.5$.

moment. Such lift characteristics due to pitching delay are also seen in symmetric pitching, e.g. the lift graph in figure 10(*a*) for $\omega^* = 0.51$.

It is also interesting to compare the $m^* = 5$ case here with the rigid case with symmetric pitching since the former has a similar effective pitching angle due to the compensation from the wing deformation. Comparing the lift graph in figure 13(*d*) and that of the rigid case in figure 11(*a*), we see that even though the two cases have a comparable peak lift, the flexible wing does not produce much lift during the early stage of a half-stroke. This difference can be explained by the chord deformation and effective pitching of this flexible wing shown in figure 13(*a*,*c*), where the combined active and passive pitching motions at that moment cause the trailing edge to pitch up, negating the positive lift from the wing translation.

Next, we examine the results for advanced active pitching. The instantaneous deformation of the chord at mid-span, the effective pitching angle, and the lift coefficient are shown in figure 14 for $m^* = 0.5$, 5 and $\omega^* = 0.36$. From figure 14(*c*), we see that the effective pitching for $m^* = 5$ is further advanced and the maximum pitching angle happens almost immediately after stroke reversal. For $m^* = 0.5$, the effective pitching angle is delayed at stroke reversal, but during wing translation the effective pitching angle is in phase with the active pitching angle. The lift data plotted in figure 14(*d*) show that the peak lift for the case of $m^* = 5$ is advanced and much higher compared to the peak lift of the rigid case, while a significant delay is found

https://doi.org/10.1017/jfm.2011.543 Published online by Cambridge University Press

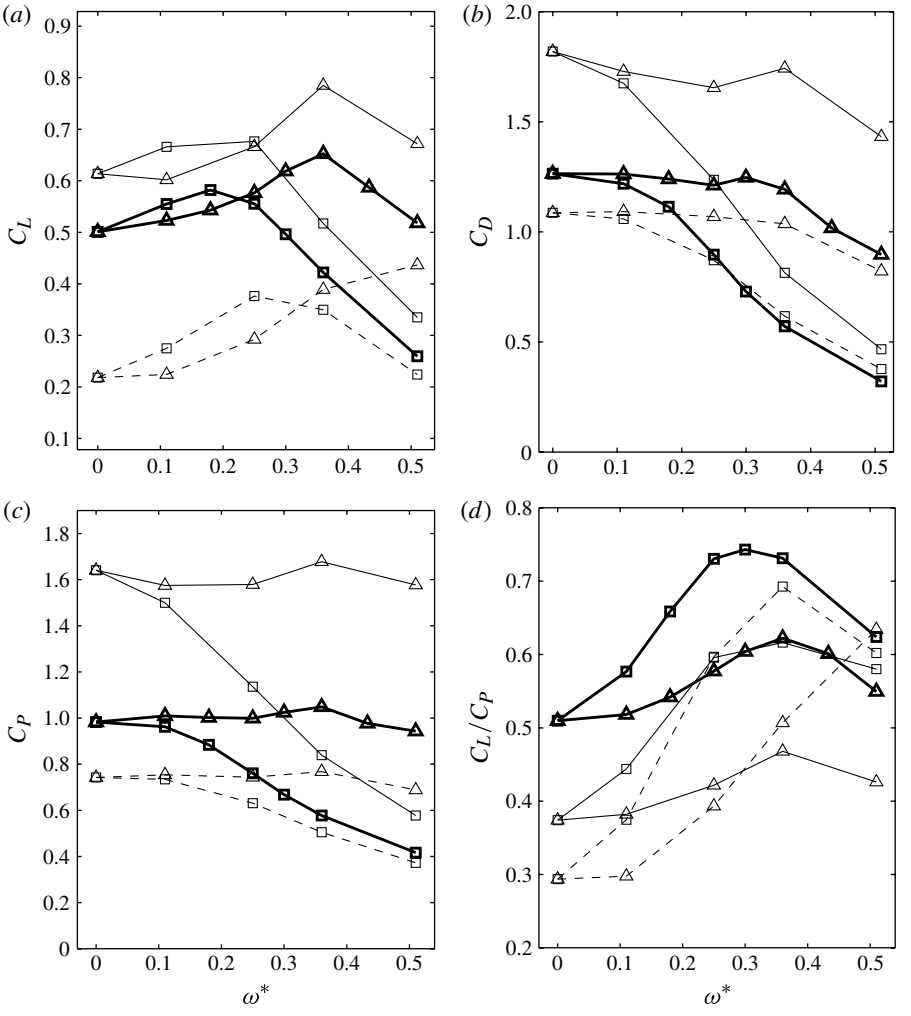


FIGURE 15. Mean lift (*a*), drag (*b*), power (*c*), and lift-to-power (*d*) coefficients for advanced (thin solid lines) and delayed pitching (dashed lines) where $m^* = 0.5$ (squares) and $m^* = 5$ (triangles). The corresponding cases with symmetric pitching are re-plotted here as thick solid lines for comparison.

for the case of $m^* = 0.5$. Negative lift is found for both flexible cases, especially for $m^* = 5$, where the inertial torque causes the wing to pitch too much toward the end of the stroke.

The time-averaged lift, drag, power, and lift-to-power coefficients for both advanced and delayed pitching are plotted in figure 15 for mass ratios $m^* = 0.5$ and 5 and for a sequence of frequency ratios. Overall, advanced pitching leads to much higher lift, drag, and power than delayed pitching. Note that the graphs for symmetric pitching shown in figure 12(*a–c*) would fall roughly between those for advanced and delayed pitching here. For both delayed and advanced pitching, moderate wing flexibility may significantly increase the lift regardless of the mass ratio, which is consistent with symmetric pitching. In addition, the wing flexibility at the low mass ratio leads to a much lower aerodynamic power than the rigid case, while the power consumption at the high mass ratio is comparable with that of the rigid case. As a result, all the

https://doi.org/10.1017/jfm.2011.543 Published online by Cambridge University Press

flexible cases have higher lift-to-power efficiency than the corresponding rigid case, no matter whether the active pitching is delayed or advanced.

Comparing the effect of the mass ratio as shown in figures 12 and 15, we see several common features among symmetric, delayed, and advanced pitching. First, the case of $m^* = 5$ has a slightly lower lift than the case of $m^* = 0.5$ at low frequency ratios but has a much higher lift at large frequency ratios. Second, the high mass ratio also corresponds to a higher drag and thus greater power requirement. Third, the net gain for $m^* = 5$ as measured by the lift-to-power ratio turns out to be lower than that for $m^* = 0.5$ for most of the cases. One exception is in figure 15(*d*), where for the case with $m^* = 5$ and delayed pitching, the power efficiency increases nearly monotonically as ω^* is raised and is even higher than that of $m^* = 0.5$ when $\omega^* = 0.51$. As discussed earlier, the passive pitching in this case has compensated the delayed active pitching, rendering an almost symmetric wing motion.

Finally, by comparing figures 15(*d*) and 12(*d*), we notice that symmetric pitching generally leads to the highest lift efficiency at constant mass and frequency ratios.

4.4. *Vortical structures*

Vortex structures are visualized by plotting the isosurface of the maximal imaginary part of complex eigenvalues of the velocity gradient tensor, Λ_{ci}. This quantity has been used previously to capture the topological flow patterns in a 3D flow field (e.g. Dong *et al.* 2006). Figure 16 shows the vortex evolution during a half-cycle for the case of $m^* = 1$, $\omega^* = 0.36$ and $\varphi = 0$. From the flow field we can identify a few major vortical structures. First, the leading-edge vortex (LEV) can be seen formed on the back side of the wing, and along the leading edge, it becomes stronger from the wing base to a location near the tip. The LEV is captured by the wing after the wing reversal and thus interacts with the wing. Second, a tip vortex (TV) is seen in the figure at, e.g. $t/T = 0.75$ and 0.85, which is formed at the tip edge of the wing and stretches into the wake as a long vortex filament. Third, a trailing-edge vortex (TEV) is formed behind the wing and is connected to the trailing edge through a thin vortex sheet. In addition to these three major vortical structures, a vortex filament is formed around the base edge of the wing and also stretches into the wake, and a semi-ring-like vortex wraps around the tip vortex filament and is formed during wing reversal near the corner between the wing tip and the trailing edge. Termed BV and CV here, these last two vortical structures are greatly affected by the particular choice of the rectangular wing shape in the current study. These vortices are connected to each other and form a vortex loop during wing translation. During wing reversal, these vortices would be shed from the wing surface, except that a large portion of the LEV away from the tip would remain connected to the leading edge. Overall, the vortices pinched off from the wing travel in the negative z-direction along with the net downwash flow. The vortex loop seen here is a typical flow feature observed previously for low-aspect-ratio rigid flapping foils (e.g. Triantafyllou, Techet & Hover 2004; Taira & Colonius 2009) (also see figure 2). One major difference in the present study is that the wing flaps by rotating around a pivot point, while in previous studies the wing motion is uniform along the span. As a result, the BV here is much weaker than the TV. Furthermore, since the present wing is performing a hovering motion and there is no free-stream flow, the vortex loop is disrupted by the wing after reversal. For a pitching/heaving foil in a free stream, the vortex loops would be convected away from the foil, and those vortices from consecutive flapping cycles would be typically interconnected (e.g. Triantafyllou *et al.* 2004).

https://doi.org/10.1017/jfm.2011.543 Published online by Cambridge University Press

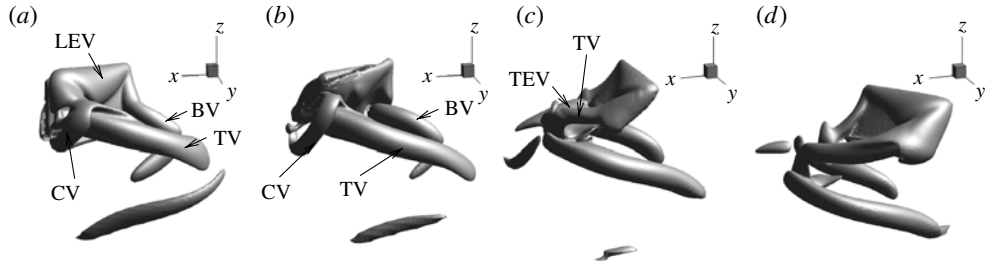


FIGURE 16. Vortical structures for $Re = 176$, $m^* = 1$, $\omega^* = 0.36$ and $\varphi = 0$ at $t/T =$ (*a*) 0.5 (stroke reversal), (*b*) 0.6, (*c*) 0.75 (mid-stroke), and (*d*) 0.85. The contour level is $10U/c$.

In figure 17, we show the vortical structures in the flow for a rigid case and two flexible cases with $m^* = 0.5$, 5 and $\omega^* = 0.36$. Symmetric pitching is used in these cases. Both mid-stroke and wing reversal are shown. Overall, the major vortices in these three cases have a similar topology. However, differences in the evolution and shedding of these vortices can be observed by inspecting the temporal series of the plots, and these differences are related to the dynamic deformation of the wing. For example, in the case of $m^* = 5$ and $\omega^* = 0.36$, the downward pitching of the trailing edge due to the elastic recovery causes the trailing-edge vortex to roll up quickly, which corresponds to the high lift prior to the mid-stroke. In comparison, the wing with $m^* = 0.5$ has a smaller effective angle of attack and a lower effective pitching rate during wing acceleration, and the appearance and subsequent development of the trailing-edge vortex are significantly delayed, which is consistent to the low lift production of this case. Since wing reversal is advanced for $m^* = 5$ and $\omega^* = 0.36$, vortex shedding from the trailing edge, which corresponds to wing reversal, is also expedited. Among the three cases, the rigid wing has the strongest tip vortex, which has led to the high drag and low power efficiency of this case. A close examination of the flow field also shows that in the flexible cases the leading-edge vortex is more attached to the back side of the wing due to the reverse camber. As the last observation for figure 17, the case of $m^* = 0.5$ in general has better organized vortices and simpler wake structures compared to the other two cases, which is consistent to the high power efficiency of this case in transferring momentum from the wing to the fluid.

Figure 18 shows the corresponding flow field in a horizontal plane and the spanwise velocity during mid-stroke for the rigid case and the case with $m^* = 0.5$ and $\omega^* = 0.36$. Comparing the two cases, we notice that for the rigid wing there is a consistent spanwise flow along much of the wingspan, while the spanwise flow is concentrated near the wing tip for the flexible wing. To explain the phenomenon, we point out that the warped surface of the flexible wing has an impedance effect on the spanwise flow. In addition, the larger deformation of the wing tip reduces the difference in the actual velocity between the tip edge and the base edge. As a result, these is less need for the fluid to move toward the tip to compensate an otherwise void space created due to the wing displacement. To conclude, the 3D wing deformation may have a significant effect on the spanwise flow of a flapping wing.

4.5. *Effect of the Reynolds number*

As a final topic, we investigate the influence of the Reynolds number. For this purpose, we set $Re = 500$ and 1000 and run selected cases on the high-resolution grid discussed

https://doi.org/10.1017/jfm.2011.543 Published online by Cambridge University Press

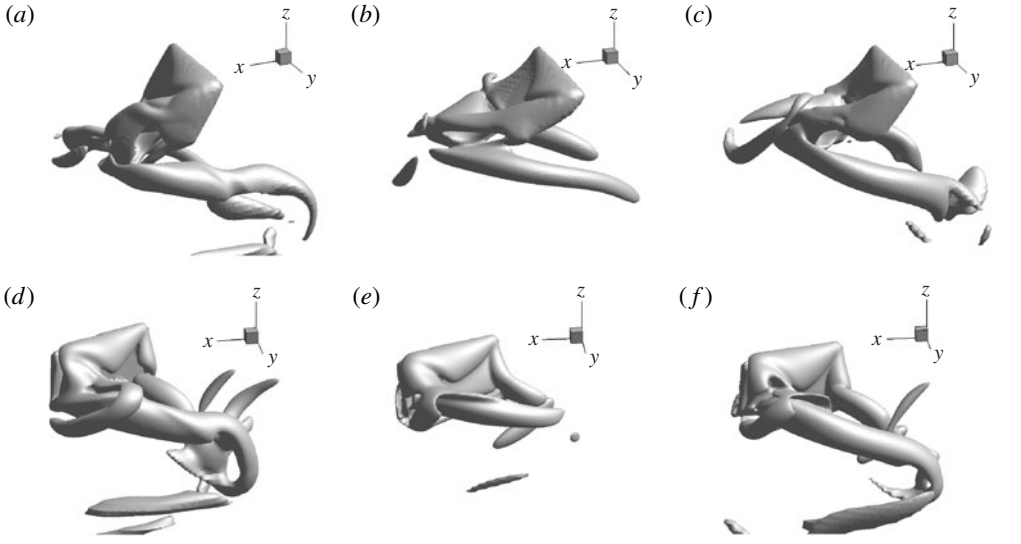


FIGURE 17. Vortical structures for (*a,d*) the rigid case, (*b,e*) $m^* = 0.5$ and $\omega^* = 0.36$ and (*c,f*) $m^* = 5$ and $\omega^* = 0.36$, $\varphi = 0$ and $Re = 176$ during (*a–c*) mid-stroke and (*d–f*) wing reversal. The contour level is $10U/c$.

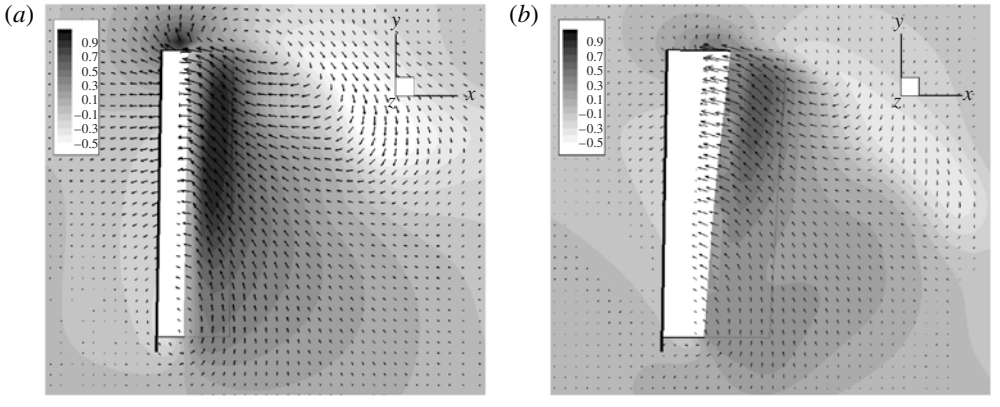


FIGURE 18. Top view of the velocity field in the plane $c/3$ below the leading edge (thick line) for (*a*) the rigid case and (*b*) $m^* = 0.5$ and $\omega^* = 0.36$, $\varphi = 0$ and $Re = 176$ during mid-stroke. Vectors at every three points are shown, and the contours represent the y-velocity component.

in the grid convergence test. At each Reynolds number, two simulations are run with $m^* = 1$ or 5 and $\omega^* = 0.36$. Figure 19 shows the flow field for the case with $Re = 500$ and $m^* = 1$. In comparison with the low-Re cases presented earlier, this case contains a much more complex wake with randomly oriented vortices. Nevertheless, some major vortical structures such as the leading-edge vortex and the long vortex filaments stretched from the tip vortex and the base vortex can be still clearly identified. The other major vortices develop finer-scale irregularities during their formation and once pinched off from the wing, they soon break up into smaller vortices spread in the wake.

https://doi.org/10.1017/jfm.2011.543 Published online by Cambridge University Press

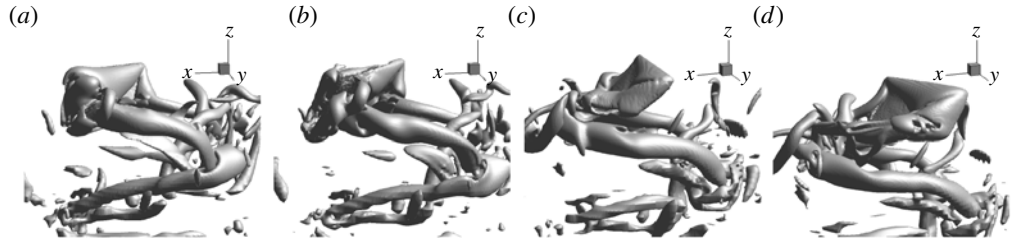


FIGURE 19. Vortical structures for $Re = 500$, $m^* = 1$, $\omega^* = 0.36$ and $\varphi = 0$ at $t/T =$ (*a*) 0.5 (stroke reversal), (*b*) 0.6, (*c*) 0.75 (mid-stroke), and (*d*) 0.85. The contour level is $10U/c$.

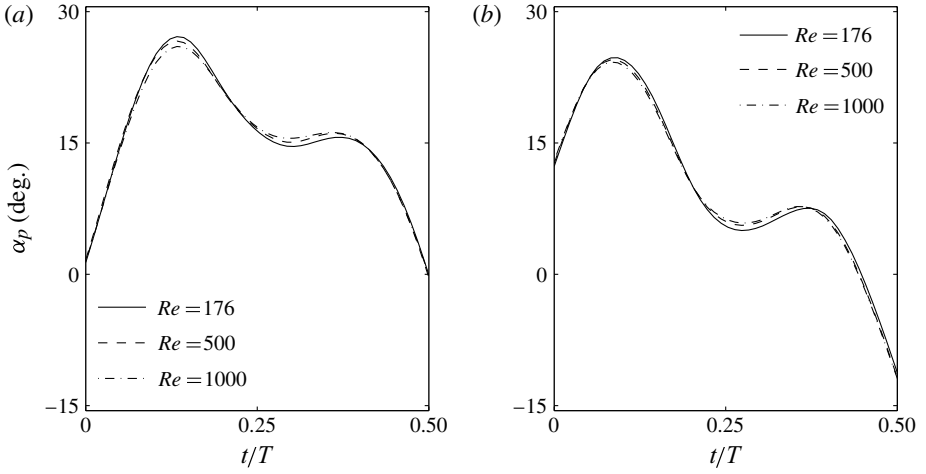


FIGURE 20. Effect of the Reynolds number on the passive pitching angle at mid-span for (*a*) $m^* = 1$ and (*b*) $m^* = 5$, $\omega^* = 0.36$ and $\varphi = 0$.

	Re	C_L	C_D	C_P	C_L/C_D	C_L/C_P
$m^* = 1$	176	0.54	0.83	0.78	0.64	0.69
	500	0.60	0.81	0.76	0.74	0.78
	1000	0.62	0.79	0.75	0.79	0.83
$m^* = 5$	176	0.66	1.23	1.07	0.54	0.62
	500	0.72	1.23	1.07	0.58	0.67
	1000	0.74	1.22	1.08	0.61	0.69

TABLE 2. Comparison of the aerodynamic performance at different Reynolds numbers, where $\omega^* = 0.36$ and $\varphi = 0$.

The effect of the Reynolds number on the wing deformation is shown in figure 20 by plotting the passive pitching angle at mid-span for both $m^* = 1$ and 5. It can seen that at $Re = 500$ and 1000, the deformation of the wing chord is quite close to that in the case of $Re = 176$. In particular, for the high mass ratio, $m^* = 5$, the Reynolds number has only a slight effect on the dynamics of the wing due to the relatively low influence of the fluid forces.

https://doi.org/10.1017/jfm.2011.543 Published online by Cambridge University Press

The effect of the Reynolds number on the aerodynamic performance of the wing is summarized by the statistics in table 2. Comparing the lift coefficient at the three Reynolds numbers from $Re = 176$ to $Re = 1000$, we see that there is a 16 % increase in C_L for $m^* = 1$ and 12 % for $m^* = 5$. For the drag and power coefficients, varying the Reynolds number has only a slight effect on the data. As a result, both the lift-to-drag and the lift-to-power ratios have increased as Re is raised. Specifically, for $m^* = 1$, C_L/C_D and C_L/C_P have grown by 22 % and 19 %, respectively, as Re goes from 176 to 1000. while for $m^* = 5$, the increments are 13 % and 11 %, respectively. Finally, we compare the two mass ratios at the same Reynolds number, and we notice that the $m^* = 5$ case has consistently higher lift and drag than the $m^* = 1$ case but the former has lower aerodynamic efficiency.

5. Conclusions

We have performed a three-dimensional simulation of the fluid–structure interaction of a low-aspect-ratio rectangular wing performing a hovering-type of flapping motion. The wing surface is clamped to a rigid leading edge and is otherwise free to deform. The numerical method features a viscous incompressible flow solver based on the immersed-boundary method and a nonlinear finite-element solver for thin-walled structures. The simulation shows that the chordwise deformation of the wing causes a dynamic pitching in addition to the active pitching applied at the wing root. The aerodynamic performance of the wing is affected not only by the increased pitching amplitude due to the deformation but also by the phase and rate of the passive pitch.

Other than the specified kinematics at the wing root and the stiffness of the wing, the dynamic pitching also largely depends on the mass ratio, which represents the relative importance of the wing inertia and aerodynamic forces in the wing deformation. At high mass ratios where the inertial torque is dominant, a phase advance is produced in the effective pitching angle during stroke reversal by the wing deformation, while at low mass ratios where the aerodynamic torque becomes equally important, a phase delay is produced during stroke reversal. During wing translation, the rate of passive pitch varies due to the combined inertial acceleration, elastic recovery, and in the case of low mass ratios, aerodynamic damping.

When $\omega/\omega_n \leqslant 0.3$, the wing deformation significantly enhances the lift production and also improves the lift efficiency although a disadvantageous camber is formed during a wing stroke. In particular, when the inertial pitching torque near wing reversal is assisted by an aerodynamic torque of comparable magnitude during wing translation, the lift efficiency can be markedly improved. This result thus confirms the insightful hypothesis by Ennos (1988*a*). Furthermore, the performance of the flexible wing is found to be consistent for different phase angles of active pitching and Reynolds numbers.

Finally, in the present study the wing-root kinematics is fixed. In the real world, insects with different wing stiffness and mass ratios could achieve their best performance by optimizing the wing-root kinematics. The wing deformation in this study is also largely limited to chordwise bending since the leading edge is rigid. However, it is reasonable to believe that the wing chord will produce a similar pitching behaviour if we allow the leading edge to twist but maintain the overall torsional stiffness of the wing. In that case, the problem of reverse camber may be alleviated.

https://doi.org/10.1017/jfm.2011.543 Published online by Cambridge University Press

Acknowledgements

This research was supported by the NSF (No. CBET-0954381). The computing resources were partly provided by the Teragrid and the Vanderbilt ACCRE. We thank Dr P. Ferreira de Sousa for helping us with one of the validation cases.

REFERENCES

BAI, P., CUI, E. & ZHAN, H. 2009 Aerodynamic characteristics, power requirements and camber effects of the pitching-down flapping hovering. *J. Bionic Engng* **6** (2), 120–134.

BATOZ, J. L., BATHE, K. J. Ü. R. & HO, L. W. 1980 A study of three-node triangular plate bending elements. *Intl J. Numer. Meth. Engng* **15** (12), 1771–1812.

BIRCH, J. M. & DICKINSON, M. H. 2001 Spanwise flow and the attachment of the leading-edge vortex on insect wings. *Nature* **412**, 729.

CHEN, J. S., CHEN, J. Y. & CHOU, Y. F. 2008 On the natural frequencies and mode shapes of dragonfly wings. *J. Sound Vib.* **313**, 643–654.

COMBES, S. A. & DANIEL, T. L. 2003 Into thin air: contributions of aerodynamic and inertial-elastic forces to wing bending in the hawkmoth manduca sexta. *J. Expl Biol.* **206**, 2999–3006.

DICKINSON, M. H., LEHMANN, F.-O. & SANE, S. P. 1999 Wing rotation and the aerodynamic basis of insect flight. *Science* **284**, 1954.

DONG, H., MITTAL, R. & NAJJAR, F. M. 2006 Wake topology and hydrodynamic performance of low-aspect-ratio flapping foils. *J. Fluid Mech.* **566**, 309–343.

DOYLE, J. F. 1991 *Static and Dynamic Analysis of Structures*. Kluwer.

DOYLE, J. F. 2001 *Nonlinear Analysis of Thin-walled Structures: Statics, Dynamic, and Stability*. Springer.

DOYLE, J. F. 2008 *QED: Static, Dynamic, Stability, and Nonlinear Analysis of Solids and Structures*. Software manual, version 4.60.

ELDREDGE, J. D., TOOMEY, J. & MEDINA, A. 2010 On the roles of chord-wise flexibility in a flapping wing with hovering kinematics. *J. Fluid Mech.* **659**, 94–115.

ELLINGTON, C. P., BERG, C. V., WILLMOTT, A. P. & THOMAS, A. L. R. 1996 Leading-dege vortices in insect flight. *Nature* **384**, 626.

ENNOS, A. R. 1988*a* The importance of torsion in the design of insect wings. *J. Expl Biol.* **140**, 137–160.

ENNOS, A. R. 1988*b* The inertial cause of wing rotation in diptera. *J. Expl Biol.* **140**, 161–169.

HEATHCOTE, S. & GURSUL, I. 2007 Flexible flapping airfoil propulsion at low Reynolds numbers. *AIAA J.* **45**, 1066–1079.

HEDRICK, T. L., CHENG, B. & DENG, X. 2009 Wingbeat time and the scaling of passive rotational damping in flapping flight. *Science* **324** (5924), 252–255.

KANG, C., AONO, H., CESNIK, C. E. S. & SHYY, W. 2011 Effects of flexibility on the aerodynamic performance of flapping wings. *AIAA Paper* 2011–3121.

KWEON, J. & CHOI, H. 2010 Sectional lift coefficient of a flapping wing in hovering motion. *Phys. Fluids* **22**, 071703.

LUO, H., DAI, H., FERREIRA DE SOUSA, P. & YIN, B. 2011 On the numerical oscillation of the direct-forcing immersed-boundary method for moving boundaries. *Comput. Fluids*, doi:10.1016/j.compfluid.2011.11.015.

LUO, H., YIN, B., DAI, H. & DOYLE, J. F. 2010 A 3D computational study of the flow–structure interaction in flapping flight. *AIAA Paper* 2010-556.

MITTAL, R., DONG, H., BOZKURTTAS, M., NAJJAR, F. M., VARGAS, A. & VON LOEBBECK, A. 2008 A versatile sharp interface immersed boundary method for incompressible flows with complex boundaries. *J. Comput. Phys.* **227** (10), 4825–4852.

PREMPRANEERACH, P., HOVER, F. S. & TRIANTAFYLLOU, M. S. 2003 The effect of chordwise flexibility on the thrust and efficiency of a flapping foil. In *Proc. 13th Intl Symp. on Unmanned Untethered Submersible Technology: Special Session on Bioengineering Research Related to Autonomous Underwater Vehicles, 24–27 August, Durham, NH.*

https://doi.org/10.1017/jfm.2011.543 Published online by Cambridge University Press

RAMANANARIVO, S., GODOY-DIANA, R. & THIRIA, B. 2011 Rather than resonance, flapping wing flyers may play on aerodynamics to improve performance. *Proc. Natl Acad. Sci.* **108** (15), 5964.

SUN, M. & TANG, J. 2002 Unsteady aerodynamic force generation by a model fruit fly wing in flapping motion. *J. Expl Biol.* **205** (17), 55.

TAIRA, K. & COLONIUS, T. 2009 Three-dimensional flows around low-aspect-ratio flat-plate wings at low Reynolds numbers. *J. Fluid Mech.* **623**, 187–207.

TRIANTAFYLLOU, M. S., TECHET, A. H. & HOVER, F. S. 2004 Review of experimental work in biomimetic foils. *IEEE J. Ocean. Engng* **29** (3), 585–594.

VANELLA, M., FITZGERALD, T., PREIDIKMAN, S., BALARAS, E. & BALACHANDRAN, B. 2009 Influence of flexibility on the aerodynamic performance of a hovering wing. *J. Expl Biol.* **212**, 96–105.

WALKER, S. M., THOMAS, A. L. R. & TAYLOR, G. K. 2010 Deformable wing kinematics in free-flying hoverflies. *J. R. Soc. Interface* **7**, 131–142.

WANG, H., ZENG, L., LIU, H. & YIN, C. 2003 Measuring wing kinematics, flight trajectory and body attitude during forward flight and turning maneuvers in dragonflies. *J. Expl Biol.* **206** (4), 745.

WANG, Z. J. 2005 Dissecting insect flight. *Annu. Rev. Fluid Mech.* **37**, 183–210.

WANG, Z. J., BIRCH, J. M. & DICKINSON, M. H. 2004 Unsteady forces and flows in low Reynolds number hovering flight: two-dimensional computations vs robotic wing experiments. *J. Expl Biol.* **207**, 449–460.

WOOTTON, R. J. 1981 Support and deformability in insect wings. *J. Zool.* **193** (4), 447–468.

WOOTTON, R. J. 1992 Functional morphology of insect wings. *Annu. Rev. Entomol.* **37** (1), 113–140.

YIN, B. & LUO, H. 2010 Effect of wing inertia on hovering performance of flexible flapping wings. *Phys. Fluids* **22**, 111902.

https://doi.org/10.1017/jfm.2011.543 Published online by Cambridge University Press